Extended State Observer-Based Force Tracking Control for Magnetorheological Dampers

Chao Ma
Department of Control Science and Engineering
Jilin University
Changchun, China
machao24@mails.jlu.edu.cn

Shuyou Yu*
National Key Laboratory of Automotive Chassis Integration and Bionics
Jilin University
Changchun, China
shuyou@jlu.edu.cn

Jie Guo
Department of Control Science and Engineering
Jilin University
Changchun, China
jieguo20@mails.jlu.edu.cn

Baojun Lin
Department of Communication Engineering
Jilin University
Changchun, China
linbj@jlu.edu.cn

***Abstract*—To address the strong nonlinearity of the magnetorheological (MR) damper and its sensitivity to environmental variations, a force-tracking control strategy based on an extended state observer (ESO) is proposed in this paper. First, based on the input-output data of the MR damper, a Hammerstein model is developed to accurately characterize its nonlinear dynamics, including typical saturation-hysteresis characteristics and energy dissipation behavior. Subsequently, a cascade control structure is designed, integrating an inverse-model feedforward controller and an ESO-based sliding mode feedback controller. By incorporating a disturbance-compensation mechanism, precise tracking of the desired damping force is achieved. Finally, simulation results confirm the effectiveness of the proposed control strategy.**

***Index Terms*—Magnetorheological damper, Hammerstein model, extended state observer, sliding mode control.**

I. Introduction

As an intelligent material, MR fluid consists primarily of magnetizable particles dispersed in a carrier fluid, supplemented with thixotropic additives, anti-wear agents, and antioxidants [1,2]. In the absence of a magnetic field, the fluid behaves approximately as a Newtonian liquid. Once a field is applied, the particles align into chain-like structures, drastically altering its rheological properties [3]. Higher excitation currents enhance particle alignment and increase the induced yield stress [4,5]. With a typical response time of 8-10 ms, MR dampers have found applications not only in suspensions but also in medical devices, seismic isolation, robotics, and other fields [6-8].

The damping response of MR dampers exhibits strong nonlinearity and time-varying characteristics due to multi-factor coupling [9], which presents significant challenges for accurate dynamic modeling. Commonly used modeling approaches can be broadly categorized into parametric and non-parametric models [10]. Parametric models include Bingham model [11], Bou--Wen model [12,13], phenomenological models [14], Dahl model [15], Sigmoid model [16], and nonlinear models based on hyperbolic tangent functions [17], among others. These models can effectively reproduce the nonlinear hysteretic behavior of MR dampers, but is often challenged by the need for precise identification of numerous parameters. Non-parametric models, in contrast, transcend the limitations of traditional mechanistic modeling by adopting a data-driven approach to directly establish the nonlinear mapping between inputs and outputs [18], thereby offering greater adaptability and flexibility. Typical examples include neural network models [19] and fuzzy models [20], with neural networks receiving particular research attention due to their strong nonlinear approximation capability and adaptive learning characteristics.

Recent studies underscore the important influence of temperature on MR fluid performance [21,22]. To address this, Savaia et al. proposed a Hammerstein-Wiener model and Guanqun Liang et al. [23] later developed a parametric hyperbolic hysteresis model with temperature as an independent variable. These methods, however, depend on extensive temperature-dependent experimental data that are often difficult to obtain. Moreover, inverse-model controllers are commonly employed for current determination, but their practical implementation is hindered by the complexity and limited accessibility of the inverse models derived from temperature-sensitive formulations [21,23]. Additional challenges, such as property degradation due to particle sedimentation during storage, further contribute to model mismatch.

Recent studies have further shown that accurate hysteresis modeling and robust force tracking of MR dampers remain active research topics. For example, Li et al. proposed a multi-stage hysteresis model for MR dampers [24], while Yu et al. developed a Hammerstein-model-based cascaded control strategy in which a neural network is used to describe the nonlinear hysteresis module and a linear model is used to represent the dynamic block [25].

To address the issues of strong nonlinearity, hysteresis, and

This work was supported in part by the National Natural Science Foundation of China (No.62473167), and the Natural Science Foundation of Jilin Province (No.20240402079GH). *Corresponding author: Shuyou Yu.

environmental sensitivity in MR dampers, a cascaded control strategy based on a Hammerstein model is proposed in this paper. Within this framework, modeling errors and external disturbances are unified as a lumped disturbance and actively compensated to ensure stable output of the desired damping force. First, a recurrent neural network (RNN) is used to construct the Hammerstein model, accurately describing the hysteretic nonlinearity of the damper. On this basis, a damping-force tracking control architecture is designed, combining an inverse model controller in series with an ESO-based sliding-mode controller. Through disturbance observation and real-time compensation, precise regulation and dynamic tracking of the desired damping force are achieved. Finally, simulations are conducted to validate the effectiveness of the proposed approach.

The main contributions are threefold: a control-oriented Hammerstein-type model is established for the MR damper; a cascade force-tracking controller is developed by combining neural-network inverse compensation and ESO-based sliding mode feedback; and the stability and tracking performance of the proposed controller are verified under different reference signals.

II. Model description and problem statement

The inherent nonlinearities and significant sensitivity of MR dampers to environmental factors substantially undermine precise modeling and force-tracking control. To address these challenges, we first characterize the damping nonlinearities based on input-output data analysis. Subsequently, a Hammerstein model is identified from experimental data to capture the nonlinear dynamics of the damper. This model provides a structured basis for designing and implementing robust force-tracking control.

A. Evaluation of MR damper characteristics

The operation of the MR damper is governed by the field-induced chain alignment of its particles, allowing rapid transition from a fluid-like state (de-energized, Fig.1(a)) to a semi-solid state (energized, Fig.1(b)), thereby providing a controllable damping force. This working principle is inherently associated with nonlinear hysteresis and dynamic saturation, which present significant challenges for high-precision control.

(a) De-energized (b) Energized

Fig. 1. Diagram of the MR Fluid Working Mechanism.

In order to acquire the input-output data of the MR damper, sinusoidal excitation is applied to a Lord RD-8041-1 damper across maximum piston velocities of 0.052, 0.131, 0.262 and 0.524 m/s, with the input current varied from 0 to 1 A in 0.1

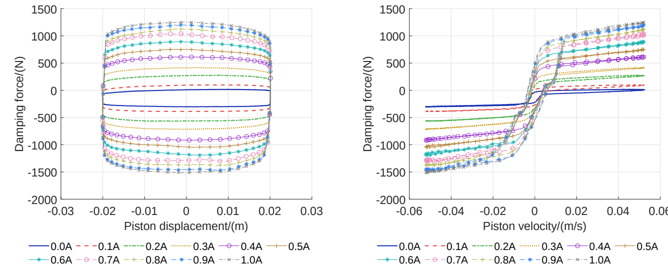

(a) Displacement-Force (b) Velocity-Force

Fig. 2. MR Damper Characteristics at a Maximum Piston Velocity of 0.052m/s.

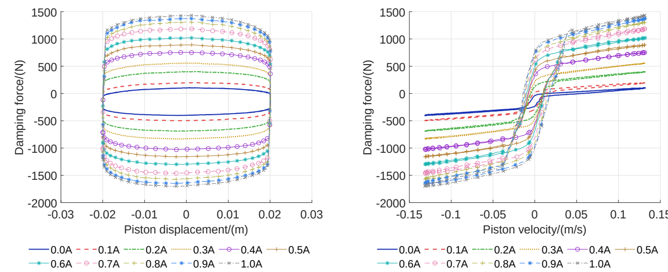

(a) Displacement-Force (b) Velocity-Force

Fig. 3. MR Damper Characteristics at a Maximum Piston Velocity of 0.131m/s.

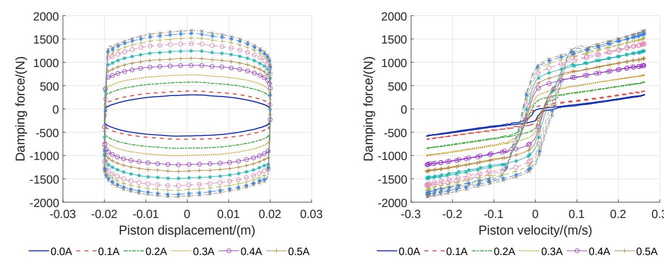

(a) Displacement-Force (b) Velocity-Force

Fig. 4. MR Damper Characteristics at a Maximum Piston Velocity of 0.262m/s.

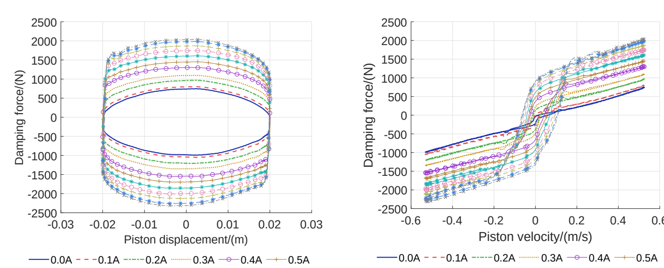

(a) Displacement-Force (b) Velocity-Force

Fig. 5. MR Damper Characteristics at a Maximum Piston Velocity of 0.524m/s.

A increments. The resulting damping characteristics are shown in Figs.2.

As shown in Fig.2, a distinct hysteresis characterizes the damping force versus piston velocity/displacement relationship, which is further accentuated by the progressive widening of the hysteresis loop with increased control current, demonstrating the strong nonlinearity of the damping force.

B. Hammerstein Model of MR Dampers

To accurately capture the strongly nonlinear damping characteristics of the MR damper, a Hammerstein model is established based on the aforementioned input-output data, offering distinct advantages for system analysis and control strategy design. As illustrated in Fig.6, the Hammerstein model adopts a block-oriented structure, which decouples the nonlinear and linear blocks of the system for separate representation.

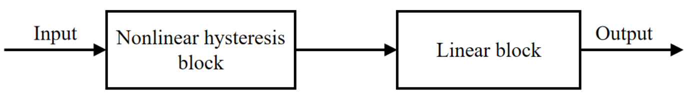

Fig. 6. Structure of the Hammerstein Model.

Nonlinear hysteresis block

The nonlinear hysteresis block of the MR damper characterizes the primary source of its damping force, i.e., the frictional force generated by the flow of MR fluid through the piston channels. This frictional force is jointly influenced by piston velocity, displacement, and the viscosity of the MR fluid, where viscosity can be dynamically regulated by adjusting the input current.

To accurately describe the nonlinear behavior of the MR damper, an RNN is adopted to establish a data-driven model for the nonlinear hysteresis component in the Hammerstein model, with the network topology shown in Fig.7. Of the experimental data, 70% is allocated for neural network training, while the remaining 30% is reserved for model validation.

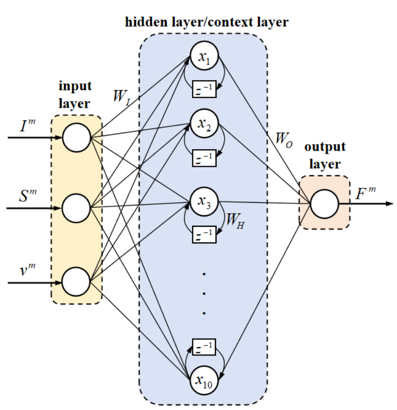

Fig. 7. Structure of the Neural Network Forward Model.

The inputs of the neural network forward model are defined as the control current I^m, the relative piston displacement S^m, the piston velocity v^m, and the output values of the hidden-layer neurons at the previous time step. The output corresponds to the damping force F^m.

Consequently, the network architecture is structured with 4 input nodes and 1 output node. The hidden layer comprises 10 neurons, a configuration determined empirically. The hyperbolic tangent (tanh) function is applied in the hidden layer to extract nonlinear features, while a linear activation function (purelin) is used in the output layer to satisfy the regression requirement for damping force prediction. The model is trained via the Levenberg-Marquardt algorithm, where the mean squared error (MSE) between the predicted and actual damping force is adopted as the loss function, thereby ensuring both high fitting accuracy and robust generalization capability.

Remark 1: To ensure the stability and convergence efficiency of the neural network training, all input and output data are normalized prior to the training process.

Linear block

A linear block is designed to compensate for system dynamic errors, mapping the predicted damping force from the nonlinear hysteresis block to the actual measured force. The derived transfer function is expressed as follows:

$$G(s) = \frac{579800}{s^2 + 671.5s + 579900} \tag{1}$$

The two poles of the transfer function model are both located in the left half of the complex plane, and the system has no zeros. Therefore, system (1) is stable.

The transfer function model (1) is transformed into a state-space representation to facilitate controller design and system analysis:

$$\begin{aligned} \begin{bmatrix} \dot{z}_1 \\ \dot{z}_2 \end{bmatrix} &= \begin{bmatrix} 0 & 1 \\ -579900 & -671.5 \end{bmatrix} \begin{bmatrix} z_1 \\ z_2 \end{bmatrix} + \begin{bmatrix} 0 \\ 1 \end{bmatrix} u \\ F_d &= \begin{bmatrix} 579800 & 0 \end{bmatrix} \begin{bmatrix} z_1 \\ z_2 \end{bmatrix} \end{aligned} \tag{2}$$

To validate the effectiveness of the Hammerstein model, simulations are conducted with a maximum piston velocity of 0.131 m/s while the current ranged from 0 to 1 A in 0.1 A increments. A comparison between the model output and the actual damping force is illustrated in Fig.8.

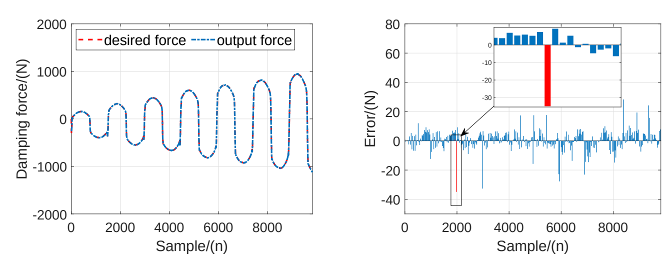

(a) Damping Force Tracking (b) Tracking Error

Fig. 8. Modeling Results of the Hammerstein Model.

As observed in Fig.8(b), the overall error between the model output and the experimental data remains within 40 N, indicating high dynamic fitting accuracy. This confirms that the constructed

Hammerstein model effectively captures the nonlinear behavior of the MR damper, thereby providing a reliable basis for subsequent controller design.

III. Control scheme

To ensure robust tracking of the desired damping force in complex or extreme environments, which are often subject to model mismatch and disturbances caused by temperature variations and parameter fluctuations that degrade the force-current mapping precision, a cascade control strategy is proposed in this section. The control structure is illustrated in Fig.9, where a neural network inverse model is used for feedforward dynamic compensation and an ESO-based sliding mode controller is integrated to provide feedback regulation for unmodeled dynamics and external disturbances.

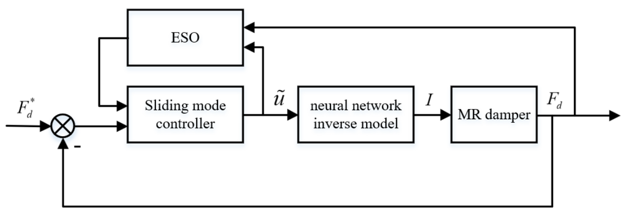

Fig. 9. Control Structure of the MR Damper Force-Tracking Control System.

A. Neural network inverse model

The neural network inverse model is primarily employed to compensate for the nonlinear characteristics of the system and to provide accurate control current commands for the MR damper. A double-hidden-layer recurrent neural network is adopted to identify the inverse model with the same recurrent structure as the forward model.

The inputs of the neural network inverse model are defined as the damping force F^m, the relative piston displacement S^m, the piston velocity v^m, and the output values of the hidden-layer neurons at the previous time step. The output corresponds to the control current I^m. Both hidden layers consist of 10 neurons each, and the activation functions remain consistent with those employed in the neural network forward model.

To validate the modeling accuracy of the inverse model, the control current tracking error is shown in Fig.11 with a maximum excitation velocity of 0.524 m/s.

Results indicate that the maximum error between the output of the neural network inverse model and the actual control current remains within 0.05 A, which verifies the effectiveness of the proposed model.

The performance of MR fluid is susceptible to external temperature variations, performance degradation, and fluctuations in system parameters, which leads to mismatch between the inverse model and the actual system. Consequently, the neural network inverse model alone is insufficient to satisfy practical control requirements. To improve the adaptability of the system to parameter disturbances and external uncertainties, a robust control strategy is additionally incorporated.

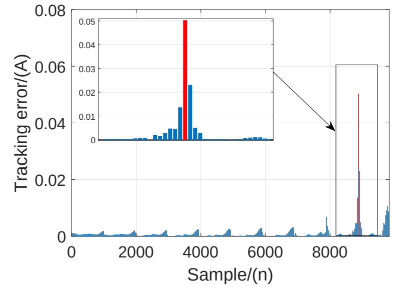

Fig. 10. Modeling Results of the Neural Network Inverse Model.

B. ESO-based sliding mode controller

1) Controller design: the detailed procedure for the ESO-based sliding mode controller is presented in the following.

It is assumed that the lumped disturbance is bounded and slowly varying within the considered operating range, which is reasonable because the MR damper operates under physically limited current, piston motion, and damping force. Define the inverse compensation error, modeling error, and related uncertainties as the total disturbance δ, system (2) is transformed into:

$$\begin{aligned} \dot{z}_1 &= z_2 \\ \dot{z}_2 &= -579900 \cdot z_1 - 671.5 \cdot z_2 + \tilde{u} + \delta \\ F_d &= 579800 \cdot z_1 \end{aligned} \tag{3}$$

where z_2 denotes the unmeasurable system state and $\tilde{u}$ is the control input.

To dynamically estimate the disturbance δ, it is further augmented as an extended system state z_3, resulting in the following expanded system:

$$\begin{aligned} \dot{z}_1 &= z_2 \\ \dot{z}_2 &= -579900 \cdot z_1 - 671.5 \cdot z_2 + z_3 + \tilde{u} \\ \dot{z}_3 &= \varphi \\ F_d &= 579800 \cdot z_1 \end{aligned} \tag{4}$$

where φ is defined as the time derivative of δ.

On the basis of the observability of the extended system (4), a Luenberger-type extended state observer can be constructed as follows:

$$\begin{aligned} \dot{\hat{z}}_1 &= \hat{z}_2 - v_1 \left(\hat{F}_d - F_d \right) \\ \dot{\hat{z}}_2 &= -579900 \cdot \hat{z}_1 - 671.5 \cdot \hat{z}_2 + \hat{z}_3 + \tilde{u} - v_2 \left(\hat{F}_d - F_d \right) \\ \dot{\hat{z}}_3 &= \varphi - v_3 \left(\hat{F}_d - F_d \right) \\ \hat{F}_d &= 579800 \cdot \hat{z}_1 \end{aligned} \tag{5}$$

Define the difference between the actual system states and the estimates provided by the observer as the observation error ℓ, and

$$\ell = \begin{bmatrix} \ell_1 & \ell_2 & \ell_3 \end{bmatrix}^{\mathrm{T}}$$

where

$$\ell_i = \hat{z}_i - z_i, \quad i = 1, 2, 3 \tag{6}$$

From the dynamics of system (4) and observer (5), it follows that the observation error (6) evolves according to:

$$\dot{\ell} = (A - vC)\ell \tag{7}$$

where

$$A = \begin{bmatrix} 0 & 1 & 0 \\ -579900 & -671.5 & 1 \\ 0 & 0 & 0 \end{bmatrix}, \quad v = \begin{bmatrix} v_1 \\ v_2 \\ v_3 \end{bmatrix},$$
$$C = \begin{bmatrix} -579800 & 0 & 0 \end{bmatrix}$$

The convergence rate of the observer state error is governed by the eigenvalues of $A - vC$, with the rate increasing as these poles are placed farther from the imaginary axis.The observer gains used in all simulations are selected as $v_1 = -1.0 \times 10^{-3}$, $v_2 = -2$, and $v_3 = -1$. The variables $\hat{z}_1$, $\hat{z}_2$, $\hat{z}_3$ represent the observed values of the system states z_1, z_2 and the disturbance z_3, respectively. $\hat{F}_d$ is the output of the observer, and v_1, v_2, v_3 are the observer gain matrices.

To ensure asymptotic stability of the error system, the gain matrix v is designed via pole placement to assign all eigenvalues of $A - vC$ to the left half-plane.

A sliding mode controller is synthesized based on the estimated system states and the observed disturbance to improve system robustness.

The linear sliding surface $\mathfrak{J}$ is defined as:

$$\mathfrak{J} = ce + \dot{e} \tag{8}$$

where c is a positive constant that satisfies the system requirements.

When the sliding condition $\mathfrak{J} = 0$ is reached and sustained, the following relationship holds between e and $\dot{e}$:

$$ce + \dot{e} \propto 0 \tag{9}$$

This implies

$$e = \exp(-ct) \tag{10}$$

which demonstrates that the tracking error e asymptotically converges to zero over time.

Define the force-tracking error as:

$$e = F_d^* - F_d \tag{11}$$

where F_d^* denotes the reference input, and F_d represents the measured output.

Consequently, the dynamics of the force-tracking error (11) are derived as:

$$\begin{aligned} \dot{e} &= \dot{F}_d^* - \dot{F}_d \\ \ddot{e} &= \ddot{F}_d^* - \ddot{F}_d \end{aligned} \tag{12}$$

Denote the estimation error of the disturbance term as:

$$\ell_3 = \hat{z}_3 - z_3 \tag{13}$$

According to eq.(2), it follows that:

$$\begin{aligned} \dot{F}_d &= 579800 \cdot \dot{z}_1 \\ \ddot{F}_d &= 579800 \cdot \ddot{z}_1 \\ \dot{z}_1 &= z_2 \\ \ddot{z}_1 &= -579900 \cdot z_1 - 671.5 \cdot z_2 + \hat{z}_3 - \ell_3 + \tilde{u} \end{aligned} \tag{14}$$

Taking the first time derivative of eq.(8), we have:

$$\begin{aligned} \dot{\mathfrak{J}} &= c\dot{e} + \ddot{e} \\ &= c\left(\dot{F}_d^* - \dot{F}_d\right) + \ddot{F}_d^* - \ddot{F}_d \end{aligned} \tag{15}$$

Substituting eqs.(12)-(14) into eq.(15) yields:

$$\begin{aligned} \dot{\mathfrak{J}} =& c\left(\dot{F}_d^* - 579800 \cdot z_2\right) + \ddot{F}_d^* \\ & - 579800 \cdot (-579900 \cdot z_1 - 671.5 \cdot z_2 + \hat{z}_3 - \ell_3 + \tilde{u}) \end{aligned} \tag{16}$$

To improve the system robustness, a reaching law with a disturbance compensation term is designed as follows:

$$\dot{\mathfrak{J}} = -\varepsilon \operatorname{sign}(\mathfrak{J}) - m\mathfrak{J} + 579800 \cdot \ell_3 \tag{17}$$

where $\operatorname{sign}(\mathfrak{J})$ is the signum function of $\mathfrak{J}$; The parameters ε and m are positive constants associated with the convergence rate.

From eqs.(16)-(17), the sliding mode control law is derived as:

$$\begin{aligned} \tilde{u} =& \frac{c\left(\dot{F}_d^* - 579800 \cdot z_2\right) + \ddot{F}_d^* + \varepsilon \operatorname{sign}(\mathfrak{J}) + m\mathfrak{J}}{579800} \\ & + 579900 \cdot z_1 + 671.5 \cdot z_2 - \hat{z}_3 \end{aligned} \tag{18}$$

Due to unmeasured system states, the sliding mode controller relies on observer-based estimates. The resulting control law is formulated as follows:

$$\begin{aligned} \tilde{u} =& \frac{c\left(\dot{F}_d^* - 579800 \cdot \hat{z}_2\right) + \ddot{F}_d^* + \varepsilon \operatorname{sign}(\mathfrak{J}) + m\mathfrak{J}}{579800} \\ & + 579900 \cdot z_1 + 671.5 \cdot \hat{z}_2 - \hat{z}_3 \end{aligned} \tag{19}$$

2) Stability analysis : the stability of the closed-loop system with the proposed controller is analyzed as follows.

Define the Lyapunov function as:

$$V = \frac{1}{2}\mathfrak{J}^2 \tag{20}$$

Taking the time derivative of eq.(20) yields:

$$\begin{aligned} \dot{V} &= \mathfrak{J}\dot{\mathfrak{J}} \\ &= \mathfrak{J}\left(-\varepsilon \operatorname{sign}(\mathfrak{J}) - m\mathfrak{J} + \ell_3\right) \\ &= -\varepsilon|\mathfrak{J}| - m\mathfrak{J}^2 + \mathfrak{J} \cdot \ell_3 \\ &= -|\mathfrak{J}|\left(m|\mathfrak{J}| + \varepsilon - |\ell_3|\right) \end{aligned} \tag{21}$$

Assuming that $\varepsilon > |\ell_3| + \vartheta$, where ϑ is an arbitrary positive constant, and both parameters $\varepsilon > 0$ and $m > 0$, then from eq.(21) we have $\dot{V} < 0$. Consequently, the system states converge to the sliding surface.

IV. Simulation analysis

To verify the effectiveness of the proposed ESO-based sliding mode control strategy, a damping force tracking control simulation is conducted. The total disturbance comprises the compensation error and the modeling inaccuracies induced by variations in MR fluid properties, is defined as follows:

$$\delta(t) = -\frac{1}{4\pi}\cos(4\pi t)\text{kN} \tag{22}$$

To evaluate the effectiveness of the proposed controller across varying dynamic conditions, reference signals consisting of step, single-frequency sinusoidal, composite sinusoidal, and triangular waves are applied-representing step response, specific frequency tracking, complex excitation response, and rapid change scenarios, respectively. Simulation results are presented in Figs.12-15, with the red solid line in each error curve denoting the maximum error under the corresponding condition. Table I further summarizes the maximum error and root mean square error (RMSE) for each reference signal to quantify the force-tracking performance.

TABLE I
MAXIMUM ERROR AND RMSE OF DAMPING FORCE TRACKING FOR VARIOUS SIGNALS

Reference signal	Maximum error (N)	RMSE (N)
Step	0.0091	0.0047
Sinusoidal	16.2116	11.3907
Composite sinusoidal	18.1810	6.8495
Triangular wave	0.4020	0.3943

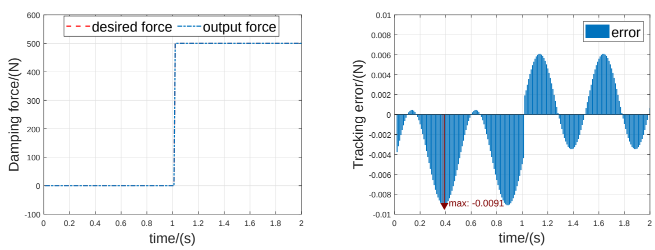

(a) Damping Force Tracking (b) Tracking Error

Fig. 11. Response to Step Signal.

As shown in Fig.12, the system responds rapidly to step inputs, with the tracking error consistently bounded within 0.0091N and an RMS error of 0.0047N. These results demonstrate both fast dynamics and high tracking precision of the controller.

Consider a single-frequency sinusoidal signal expressed as:

$$y^*(t) = 2.5\sin(2\pi f t)\mathrm{kN} \tag{23}$$

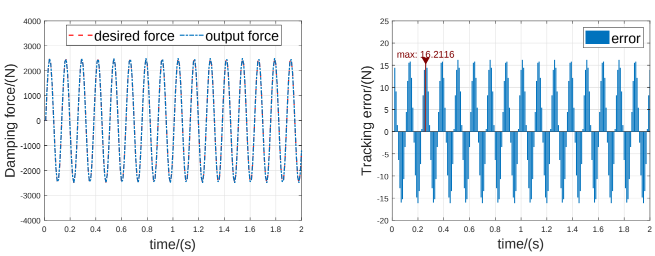

(a) Damping Force Tracking (b) Tracking Error

Fig. 12. Response to Single-Frequency Sinusoid Signal.

As shown in Fig.13, with the frequency set to 8 Hz, the maximum tracking error and the RMSE are 16.2116 N and 11.3907 N, respectively, both of which remain within a reasonable range.

A composite frequency signal is defined as:

$$\begin{aligned} y^*(t) =& 1 - 1.5\sin \\ & \left(2 - \cos\left(2\pi f_1 t\right) - \cos\left(2\pi f_2 t\right) - \cos\left(2\pi f_3 t\right)\right)\mathrm{kN} \end{aligned} \tag{24}$$

The frequencies are set to f_1=5 Hz, f_2=8 Hz, and f_3=12 Hz, respectively. The simulation results are shown in Fig.14.

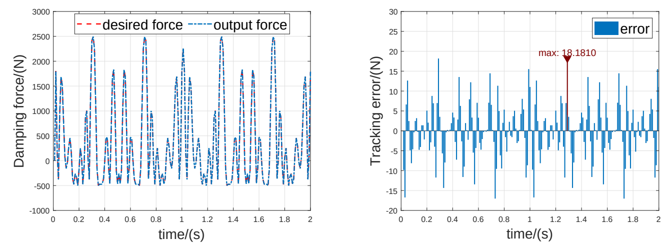

(a) Damping Force Tracking (b) Tracking Error

Fig. 13. Response to Composite Frequency Sinusoid Signal.

For the composite frequency signal, the maximum and RMSE are 18.1810 N and 6.8495 N, respectively. This indicates that the proposed ESO-based sliding mode controller maintains both high tracking accuracy and robust dynamic stability.

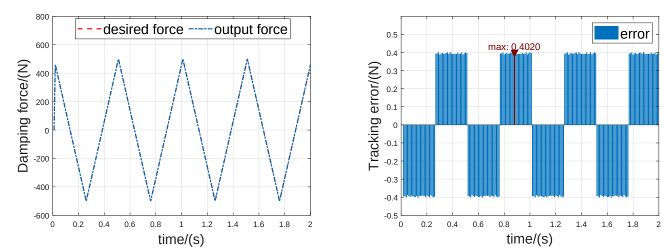

(a) Damping Force Tracking (b) Tracking Error

Fig. 14. Response to Triangular Wave Signal.

As shown in Fig.15 for the triangular wave signal, the controller demonstrates strong performance, boasting a maximum tracking error of 0.4020 N and an RMSE of 0.3943 N. These results validate its strong adaptability and effectiveness in handling non-smooth inputs.

In summary, the proposed ESO-based sliding mode control synthesizes unmodeled dynamics and external disturbances into a single total disturbance term and actively compensates for it in real time, thereby ensuring high-precision force tracking and robust performance under complex excitations.

Remark 2: The sinusoidal signal causes a larger tracking error due to its higher frequency content.

Remark 3: The sliding mode control law requires the first and second derivatives of the desired damping force. In the present simulation, these derivative signals are obtained under ideal conditions. In future work, related differentiator methods [26], [27] will be considered, and testbed will be carried out to further verify the real-time force-tracking performance of the proposed controller.

V. Conclusion

The established Hammerstein model effectively captured the nonlinear dynamic characteristics of the MR damper, while maintaining a balance between modeling accuracy and computational complexity. Based on this model, a cascade control strategy was proposed. In this strategy, an inverse hysteresis model was utilized in the feedforward path to compensate for the nonlinearity of the MR damper. Concurrently, an ESO-based sliding mode controller was introduced to strengthen the robustness of the system against inverse compensation errors, model uncertainties, and external disturbances. Simulation results demonstrated that the proposed control scheme maintained high tracking accuracy while exhibiting good robustness.

References

[1] W. Xu, Y. K. Hu, Y. K. Zhang, and J. Y. Wang, “Design of An Integrated Magnetorheological Fluid Brake Axial Flux Permanent Magnet Machine,” IEEE Transactions on Transportation Electrification, vol. 10, no. 1, pp. 1876-1886, 2023.

[2] R. Asiaban, H. Khajehsaeid, E. Ghobadi, and M. Jabbari, “New magnetorheological fluids with high stability: Experimental study and constitutive modelling,” Polymer Testing, vol. 87, pp. 106512, 2020.

[3] T. Plachy, M. Cvek, Z. Kozakova, M. Sedlacik, and R. Moucka, “The enhanced MR performance of dimorphic MR suspensions containing either magnetic rods or their non-magnetic analogs,” Smart Materials and Structures, vol. 26, no. 2, pp. 025026, 2017.

[4] A. Raju, S. Choi, and M. Ferdaus, “A state of art on magneto-rheological materials and their potential applications,” Journal of Intelligent Material Systems and Structures, vol. 29, no. 10, pp. 2051-2095, 2018.

[5] P. John, “Magnetic nanofluids (Ferrofluids): Recent advances, applications, challenges, and future directions,” Advances in Colloid and Interface Science, vol. 311, pp. 102810, 2023.

[6] L. Deng, S. S. Sun, M. Christie, D. H. Ning, S. D. Jin, H. P. Du, et al, “Investigation of a seat suspension installed with compact variable stiffness and damping rotary magnetorheological dampers,” Mechanical Systems and Signal Processing, vol. 171, pp. 108802, 2022.

[7] R. Sharma, P. Gaur, S. Bhatt, and D. Joshi, “Performance Assessment of Fuzzy Logic Control Approach for MR-Damper Based-Transfemoral Prosthetic Leg,” IEEE Transactions on Artificial Intelligence, vol. 3, no. 1, pp. 53-66, 2022.

[8] M. Kennard, K. Yagi, M. Hassan, H. Kadone, H. Mochiyama and K. Suzuki, “Variable-Damper Control Using MR Fluid for Lower Back Support Exoskeleton,” IEEE/ASME Transactions on Mechatronics, vol. 28, no. 1, pp. 579-587, 2023.

[9] H. Zhang, K. Cheng, E. Wang, S. Rakheja and C. Y. Su, “Nonlinear Behaviors of a Half-car Magneto-Rheological Suspension System under Harmonic Road Excitation,” IEEE Transactions on Vehicular Technology, 2023.

[10] Q. Bui, X. Bai, and Q. Nguyen, “Dynamic modeling of MR dampers based on quasi–static model and Magic Formula hysteresis multiplier,” Engineering Structures, vol. 245, pp. 112855, 2021.

[11] P. Changle, C. Cheng, and H. Hetao, “Parameter uncertainty analysis of MNS model for magneto-rheological damper,” Engineering Mechanics, vol. 37, no. 1, pp. 175-182, 2020.

[12] H. T. Zhu, X. T. Rui, F. F. Yang, W. Zhu, and M. Wei, “An efficient parameters identification method of normalized Bouc-Wen model for MR damper,” Journal of Sound and Vibration, vol. 448, pp. 146-158, 2019.

[13] T. Kumar, R. Kumar, and S. Jain, “Numerical investigation of semi-active torsional vibration control of heavy turbo-generator rotor using magnetorheological fluid dampers,” Journal of Vibration Engineering and Technologies, vol. 9, no. 5, pp. 967-981, 2021.

[14] J. Guo, Z. Li, and M. Zhang, “Parameter identification of the phenomenological model for magnetorheological fluid dampers using hierarchic enhanced particle swarm optimization,” Journal of Mechanical Science and Technology, vol. 35, no. 3, pp. 875-887, 2021.

[15] A. Tusset, F. Janzen, V. Piccirillo, R. Rocha, J. Balthazar, and G. Litak, “On nonlinear dynamics of a parametrically excited pendulum using both active control and passive rotational (MR) damper,” Journal of Vibration and Control, vol. 24, no. 9, pp. 1587-1599, 2018.

[16] H. W. Lu, Z. M. Xu, K. Z. Gao, Z. F. Zhang, Z. Li, and J.J. Xie, “A new invertible model of magnetorheological damper based on sigmoid function,” Smart Materials and Structures, vol. 29, no. 11, 2020.

[17] F. Meng, and J. Zhou, “Modeling and Control of a Shear-Valve Mode MR Damper for Semiactive Vehicle Suspension,” Mathematical Problems in Engineering, 2019.

[18] M. Kennard, K. Yagi, M. Hassan, H. Kadone, H. Mochiyama and K. Suzuki, “Variable-Damper Control Using MR Fluid for Lower Back Support Exoskeleton,” IEEE/ASME Transactions on Mechatronics, vol. 28, no. 1, pp. 579-587, 2023.

[19] S. Kumar, S. Chandramohan, and S. Sujatha, “Geometric optimization of magnetorheological damper for prosthetic ankles using artificial neural networks,” Mechatronics, vol. 98, pp. 103108, 2024.

[20] D. Zhang, H. Yuan, and Z. Cao, “Environmental adaptive control of a snake-like robot with variable stiffness actuators,” IEEE/CAA Journal of Automatica Sinica, vol. 7, no. 3, pp. 745-751, 2020.

[21] G. Savaia, M. Corno, G. Panzani, A. Sinigaglia and S. M. Savaresi, “Temperature Estimation in a Magneto–Rheological Damper,” 2020 IEEE Conference on Control Technology and Applications (CCTA), Montreal, QC, Canada, pp. 567-572, 2020.

[22] J. Song, A. Zhu, Y. Tu, C. Zheng and G. Cao, “Magnetorheological damper with variable displacement permanent magnet for assisting the transfer of load in lower limb exoskeleton,” IEEE Transactions on Neural Systems and Rehabilitation Engineering, vol. 32, pp. 43-52, 2023.

[23] G. Q. Liang, T. Zhao, N. F. Li, Y. T. Wei, and S. M. Savaresi “Magnetorheological damper temperature characteristics and control-oriented temperature-revised model,” Smart Materials and Structures, 2021.

[24] J. Li, C. Liao, L. Xie, X. Wei, X. Du, B. Gan, and M. Shou, “Multi-stage hysteresis modelling of magnetorheological dampers and experimental verification,” International Journal of Mechanical Sciences, vol. 254, Art. no. 108435, 2023.

[25] S. Yu, J. Guo, X. Xu, S. Zhang, and B. Lin, “A cascaded control strategy for magneto-rheological dampers based on Hammerstein model,” Mechanical Systems and Signal Processing, vol. 222, Art. no. 111748, 2025.

[26] J. Q. Han, “Active disturbance rejection control technique: the technique for estimating and compensating the uncertainties,” Beijing: National Defense Industry Press, 2008.

[27] Y. Gao, W. H. Wu, and L. Gao, “Linear active disturbance rejection control for high-order nonlinear systems with uncertainty,” Control and Decision, vol. 35, no. 02, pp. 483-491, 2020.